Delft University of Technology

Modeling the antifouling properties of atomic layer deposition surface-modified ceramic nanofiltration membranes

Moyo, Welldone; Chaukuraa, Nhamo ; Motsaa, Machawe M. ; Msagatia, Titus A.M. ; Mambab, Bhekie B. ; Heijman, Sebastiaan G.J.; Nkambulea, Thabo T.I.

Important note
To cite this publication, please use the final published version (if applicable).
Please check the document version above.

Modeling the antifouling properties of atomic layer deposition surface-modified ceramic nanofiltration membranes

Welldone Moyo, Nhamo Chaukura, Machawe M. Motsa, Titus A. M. Msagati, Bhekie B. Mamba, Sebastiaan G. J. Heijman & Thabo T. I. Nkambule

View supplementary material ☐

Published online: 10 Jun 2022.

Submit your article to this journal ☐

Article views: 19

View related articles ☐

View Crossmark data ☐

Taylor & Francis
Taylor & Francis Group

Check for updates

Modeling the antifouling properties of atomic layer deposition surface-modified ceramic nanofiltration membranes

Welldone Moyo[a] , Nhamo Chaukura[a], Machawe M. Motsa[a], Titus A. M. Msagati[a] , Bhekie B. Mamba[b], Sebastiaan G. J. Heijman[c] and Thabo T. I. Nkambule[a]

[a]Institute for Nanotechnology and Water Sustainability (iNanoWS), University of South Africa (UNISA), Johannesburg, South Africa; [b]College of Science, Engineering and Technology, University of South Africa (UNISA), Johannesburg, South Africa; [c]Department of Civil Engineering and GeoSciences, Technical University of Delft, Delft, The Netherlands

ABSTRACT

This work investigates the enhancement of antifouling properties of ceramic nanofiltration membranes by surface modification *via* atomic layer deposition (ALD) of TiO_2. Feed solutions containing bovine serum albumin (BSA), humic acid (HA) and sodium alginate (SA) were used as model foulants. The classic fouling mechanism models and the modified fouling indices (MFI) were deduced from the flux decline profiles. Surface roughness values of the ALD coated and uncoated membranes were 63 and 71 nm, respectively, while the contact angles were 34.2 and 59.5°, respectively. Thus, coating increased the water affinity of the membrane surfaces and consequently improved the anti-fouling properties. The MFI values and the classic fouling mechanism correlation coefficients for cake filtration for the ALD coated and the uncoated membrane upon SA fouling were 42,963 ($R^2 = 0.82$) and 143,365 sL^{-2} ($R^2 = 0.98$), respectively, whereas the correlation coefficients for the combined foulants (SA + BSA + HA) were 267,185 ($R^2 = 0.99$) and 9569 sL^{-2} ($R^2 = 0.37$), respectively. The study showed that ALD can effectively enhance the anti-fouling properties of ceramic membranes.

GRAPHICAL ABSTRACT
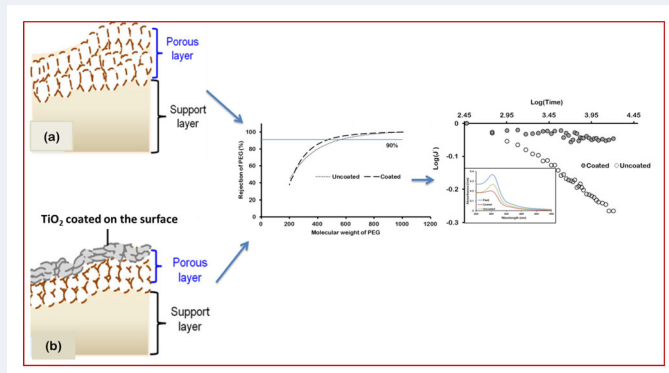
Introduction

The effectiveness of membrane separation performance is delineated by the physico–chemical properties, composition and microstructure of the active layer (Tylkowski and Tsibranska 2015). Membranes can either be derived from organic/polymeric or inorganic/ceramic materials. Polymeric membranes have been preferred because they are relatively cheaper compared to ceramic membranes. However, they suffer several limitations such as a short life span, limited recyclability and poor chemical, mechanical and thermal stability (Metsämuuronen et al. 2014). In comparison, ceramic membranes derived from metal oxides, typically zirconia, titania, alumina and more recently silicon carbide, have high selectivity and superior mechanical, thermal and chemical stability (Amin 2016). For this reason, ceramic membranes

have found applications in food processing, pharmaceutical production, petrochemical refining, chemical manufacturing and water and wastewater treatment, where the conditions can be extreme (Metsämuuronen et al. 2014). The utility of ceramic membranes is further enhanced by modifying the membrane surface and tuning the porosity through the choice of precursors and the fabrication conditions or by post modification treatments following synthesis.

Surface modifications such as pore size tuning are important for engineering the selectivity and flux of membranes. Commonly used modification methods include electroless gold deposition and polymer grafting (Sun et al. 2013; Mustafa et al. 2016). However, these methods are laborious, time consuming and involve the use of hazardous chemicals, hence their application is limited (Sun et al. 2013). Vapor deposition techniques such as physical vapor deposition (PVD), chemical vapor deposition (CVD) and atomic layer deposition (ALD) offer better alternatives for surface and pore size modification because they are not specific to the chemistry of the substrate material (Kim and Oh 2014). Moreover, the thickness of the coating can be manipulated over a wide range (Kim and Oh 2014).

Thin film layer coating *via* the ALD method involves introducing non-overlapping and alternate pulses of precursor gases or vapors and their subsequent chemisorption on the sample. Once all the reactive sites on the substrate surface are occupied, the reaction self terminates. The saturative self-limiting steps in ALD allows for one sub-monolayer growth of film per deposition cycle. Consequently, the ALD method achieves: (1) a uniform thin layer even on large surface area substrates; (2) retention of conformal integrity even on high aspect ratio structures, and (3) judicious control of film thickness. Thus, ALD is suitable for high precision surface functionalization and pore size modification of ceramic membranes. A number of materials including polymers, sulfides, metals and oxides have been deposited on ceramic membranes (Dendooven and Detavernier 2017). However, the majority of previous studies concentrated on applying ALD modification on membranes for gas separation (Park et al. 2006; Kim and Oh 2014). The application of ALD modification for the enhancement of surface hydrophilicity and antifouling properties of ceramic membranes is less studied.

Dissolved organic matter (DOM) is ubiquitous in all surface waters (Nkambule 2012). Literature reports that DOM affects the organoleptic and aesthetic properties of the produced water, and are the major membrane foulants (Motsa et al. 2018). DOM can be characterized and tracked using fluorescence and UV-Vis spectroscopy in aquatic systems (Li and Hur 2017). Besides their simplicity in application, these optical methods have the potential to predict the removal and fouling character of DOM fractions during membrane filtration. Extant literature report the severity of DOM fouling is exacerbated by hydrodynamic parameters such as cross flow velocity, transmembrane pressure (TMP), flux and recovery (Zhou and Guo 2015; Fang et al. 2018; Yu et al. 2018), and the physico–chemical characteristics of the feed stream (Kimura and Oki 2017; Motsa et al. 2018). The utility of fouling modeling tools such as the modified fouling index (MFI) has come in handy in predicting fouling behavior (De Angelis and Cortalezzi 2013; Le et al. 2018). Previous research demonstrate that the feed stream concentration is linearly proportional to MFI, and therefore the MFI tool is conjectured to describe the actual impact of the feed stream concentration on the fouling behavior observed (Le et al. 2018). Applying MFI modeling saves time and resources required to conduct pilot studies to determine pretreatment requirements. Although previous research has shown ALD modification improve the water permeability of membranes (Shang et al. 2017), to date we are not aware of studies that use the MFI tool on ALD-modified membranes to delineate the extent of fouling and the fouling mechanism. The aim of this research was to identify and model the fouling of ALD modified and uncoated ceramic membranes by single and combined DOM foulants, namely: sodium alginate (SA), bovine serum albumin (BSA) and humic acid (HA) at a laboratory scale.

Materials and methods

Materials

Analytical-grade SA (30 mg L^{-1}), BSA (20 mg L^{-1}) and HA (50 mg L^{-1}) were sourced from Sigma Aldrich, South Africa and deionized (DI) water (Millipore, USA) was used throughout for preparing solutions. The SA, BSA and HA were the model DOM fractions representing polysaccharides, proteins, and humic substances, respectively. The surface water stream was further simulated by adding magnesium chloride ($MgCl_2$), calcium chloride ($CaCl_2$), potassium chloride (KCl) and sodium chloride (NaCl) as background electrolytes to predetermine the ionic strength

of the solutions to 10 mM at room temperature. Concentrations of foulants exceeding that usually found in surface water were chosen to mimic fouling after the extended operation (Sun et al. 2016). The compositions of the various feed streams tested are shown in Table A1 (Supplementary material). The as-received commercial flat disc ceramic nanofiltration (NF) membranes with active and support layers of TiO$_2$ and Al$_2$O$_3$, respectively, (Inopor, Germany) were used in this work. The membranes had an active filtration area of 0.00563 m^2, 2.5-mm thickness, 90-mm diameter, and 30% porosity. Besides the ALD coating, the uncoated membranes were not treated further and were used as received from the supplier.

Determination of fluorescent DOM and polysaccharides

To determine the fluorescence properties of DOM model fractions, an Aquolog fluorescence spectrometer (HORIBA, USA) was used at the excitation and emission ranges of 200–800 and 248.58–830.59 nm, respectively, while the wavelength intervals, $\Delta\lambda$ were 2 and 3.28 nm, respectively. Polysaccharides were converted to UV-Vis absorbing furfural derivatives using the method by Albalasmeh et al. (2013) with modifications. In brief, to each 1 mL aliquot sample from the feed and permeates, 3 mL of 95% sulfuric acid was added. Thereafter, the mixture was vortexed for 30 s and UV-Vis absorbance was determined using a UV-Vis spectrophotometer (Lambda 650S, Perkin Elmer). The prominent peak intensity at 315 nm was assumed to be directly proportional to the concentration of polysaccharide derivatives in the sample. It must be noted that the presence of cations enhances or diminishes the UV signal depending on the complexing cation and the amount of cations complexed in the sample (Zhou et al. 2017). Therefore, the results are indicative, not absolute.

ALD surface modification of ceramic membranes

Coating of the ceramic membrane substrate with TiO$_2$ was conducted in a flow-type ALD reactor (TU Delft, The Netherlands). Demineralized water vapor and titanium tetrachloride (TiCl$_4$) (Sigma-Aldrich/Fluka, The Netherlands) were the precursors for the ALD coating experiments, and nitrogen (N$_2$) was used as the carrier gas to deliver and deposit the precursors perpendicular to the membrane surface (HiQ 5.0, The Netherlands). A digital temperature probe was used to control the ALD reactor temperature at

70 °C using an infrared lamp as a source of heat. Dry N$_2$ was used to purge the produced hydrochloric acid (HCl), unreacted precursors and residual water (H$_2$O) (Supplementary material, Figure S1). Three rounds of ALD coating were applied to maintain the pore size close to the uncoated membrane as possible so that the only variable for comparison was the coating on the membrane surface. Flat silicon wafers (20 mm × 20 mm) were used to determine the growth per cycle because their surfaces are terminated by the hydroxyl (OH) group, and mimic that of the ceramic membranes. The silicon wafers were placed next to the ceramic membrane in the ALD reaction chamber and the thickness of the coating on the silicon wafers was determined using an ellipsometer (M-2000F, J.A.Woollam Co. Inc., USA).

Characterization of the membranes, fouling analysis and operation

Ceramic membranes

The defects corrected molecular weight cut off (MWCO) for these membranes was below 5% as measured by the method developed by Kramer et al. (2019). The surface morphology and elemental mappings of the membranes were determined using a scanning electron microscope (JSM-IT300, JEOL, Tokyo, Japan) equipped with an energy dispersive spectroscope. Surface topology was determined in air using an atomic force microscope (AFM) (WITEc Focus Innovations, Germany), programmed to the contact mode. A triangular Si$_3$N$_4$ NP probe (Veeco Instruments, CA), with a nominal frequency of 20 kHz and a nominal cantilever spring constant of 0.12 Nm^{-1} was used. The tip height was adjusted to 2.5–3.5 μm, with a side angle of 35° and a nominal radius of 20 nm. On each membrane, five different sites of dimensions 20 μm × 20 μm, were scanned at a rate of 0.5 Hz and averaged. Roughness and height data were obtained using the in-built Nanoscope program (Nanoscope 5.30 r3 sr3, Veeco Instruments, CA). The water contact angles (θ) were measured using the sessile drop method. In this method, three liquids with well-characterized surface tension components, namely: Milli-Q water, diiodomethane and glycerol, were used. At least 10 drops per liquid were deposited on the membrane surface using a microlite syringe, from which the contact angle was determined. The θ was then used to calculate surface tension and interfacial free energies of interactions. Briefly, the sum of the Liftshitz-van der Waals component (γ^{LW}) and Lewis acid–base components γ^{AB}

$(\gamma^{AB} = 2\sqrt{\gamma^+ \ \gamma^-})$ with γ^+ and γ^- being the electron acceptor and electron donor, respectively was used to determine the total surface tension.

Determination of molecular weight cut off

MWCO of the ALD coated and the uncoated membranes were determined by analyzing the retention of polyethylene glycols (PEG) (0.6 gL^{-1}) (Sigma Aldrich, Germany) of average molecular weights (MW) 200–1000 Da using a high-performance liquid chromatograph (HPLC) (Shimadzu, Japan) fitted with size exclusion chromatography (SEC) columns (5 µm 30 Å) (PSS Polymer Standards Service GmbH, Germany). The rejection rates of PEG (r_{PEG}) of a specific molecular weight were used to plot the retention curves (Equation 1):

$$r_{PEG} = \frac{(C_0 - C_p)}{C_0} \tag{1}$$

where, C_0 and C_p are the concentrations of PEG in the feed and permeate, respectively.

Thereafter, the experimental rejection curves were described using a log-normal model as a function of MW and MWCO (Equation 2) (Shang et al. 2017):

$$\sigma(MW_s) = \int_0^{MW_s} \frac{1}{S_{MW}\sqrt{2\pi}} \frac{1}{MW} \exp \\ \left[\frac{-((In(MW) - In(MWCO) + 0.56S_{MW}))^2}{2S_{MW}^2} \right] \tag{2}$$

where $\sigma \ (MW_s)$ is the reflection coefficient for a PEG with a molecular weight MW_s, S_{MW} is the standard deviation of the molecular weight (MW) distribution.

Based on the premise that the separation of PEG molecules was solely through steric exclusion with insignificant solute diffusion, the MWCO was taken to be the value at which 90% of PEGs are retained (Shang et al. 2017).

Operation of filtration system

Circulation of the feed water in cross flow mode and cross flow velocity of 1 ms^{-1} was maintained by a pump operated at 1100–1180 RPM. A circular disc module was used to house the membrane (TAMI, Germany), and the positioning of the concentrate valve was used to pressurize the system. The TMP was set at 3 bars while the feed flow rate was maintained at 175 Lh^{-1}. The flow rate sample mass correlation, flux and the permeability were temperature corrected (Equations 3–6) (Shang et al. 2017):

$$v_s = \frac{(M_{SC} - M_C)}{(T_f \times 60)/1000} \tag{3}$$

$$\Delta P = \frac{P_f + P_c}{2} \tag{4}$$

$$J = \frac{v_s}{A} \tag{5}$$

$$L_{p, 20^0C} = \frac{J}{\Delta P} . \frac{\eta_T}{\eta_{20}} = \frac{J.e^{-0.0239(T-20)}}{\Delta P} \tag{6}$$

where v_s denotes the flow rate, and mass of the sample container including permeate and the mass of the empty container is denoted by M_{sc} and M_c, respectively. The temperature of water (^oC) is indicated by T_f, TMP (bar) of the system is denoted by ΔP, the feed and concentrate pressure is denoted by P_f (bar) and P_c (bar), respectively, the obtained membrane flux is indicated by J (Lm^{-2}h^{-1}). The effective membrane filtration area is described by A (m^2), the permeability at 20 °C is denoted by $L_{p,20}°C$ (Lm^{-2}h^{-1}bar^{-1}) and the permeate viscosities at 20 °C and at the measured water temperature is described by η_{20} and η_T, respectively.

Samples were withdrawn hourly for 6 h from the feed and permeate streams. The permeate flux loss and fouling behavior due to the presence of foulants was investigated in the presence of Ca^{2+}, Mg^{2+}, K$^+$ and Na$^+$.

Modified fouling index (MFI)

In-depth protocol of cross flow mode measurement of the MFI is discussed elsewhere (Koo et al. 2013; Jee et al. 2016; Le et al. 2018). In brevity, the slope of the inverse flow rate (t/V) versus the cumulative volume (V) gives the numerical value of the MFI (Equation 7) (Jee et al. 2016):

$$\frac{t}{V} = \frac{\eta R_m}{A\Delta P} + \underbrace{\frac{\eta\alpha C}{2\Delta PA^2}}_{MFI} V \tag{7}$$

where η describes the dynamic viscosity is, is the TMP (trans-membrane pressure) is denoted by ΔP, concentration of foulants in the feed is described by C, α describes the cake-specific resistance, area of the membrane is denoted by A.

The applied TMP is inversely proportional to MFI, further, MFI is directly proportional to the cake filtration fouling potential (Salinas-Rodriguez et al. 2015). Thus, the MFI tool can be used to elucidate the fouling potential of various foulant feed streams.

The rate of flux decline, m, was deduced to be the slope at the particular time range (Equation 8).
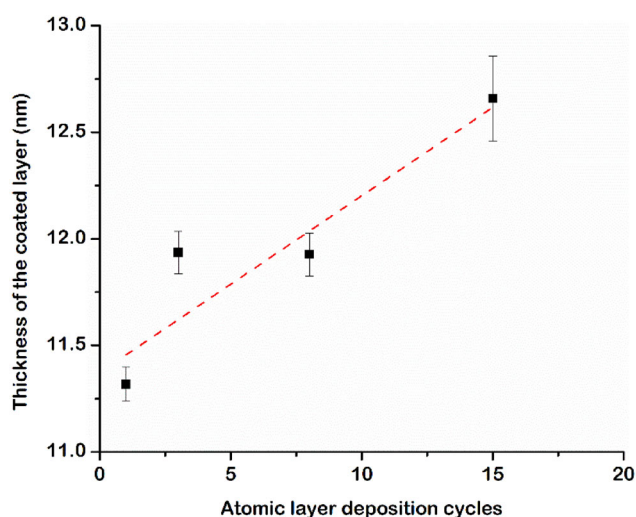
Figure 1. Growth per atomic layer deposition cycle on a silicon wafer.

$$m = \frac{dj}{dt} \qquad (8)$$

where j and t represent the log transformed flux and time, respectively.

Supplementary information (Box A1) describes the fouling mechanism models used in this study (De Angelis and Cortalezzi 2013). The graphs were generated by plotting time versus a function of flux, consecutive points on a graph presenting a linear segment (explained by R^2) denoted the different mechanisms, namely complete blocking, standard blocking, intermediate blocking and cake filtration.

Statistical analysis. The Tukeys's mean comparison and one-way ANOVA tests ($p \leq 0.05$) (SPSS, IBM Inc) were used to determine the statistical significance of the differences in the measured surface roughness values for the uncoated and coated membrane.

Results and discussion

Growth dynamics of TiO_2 on the surface of the silicon wafer

The growth per cycle (GPC) of TiO_2 was linearly correlated with incremental ALD cycles ($R^2 = 0.85$) (Figure 1). The GPC obtained from the gradient of the linear regression was 0.08 nm per cycle. However, the thickness or growth of subsequent layers and the number of ALD cycles did not follow a linear correlation because from 1 to 3 ALD cycles. The growth rate was higher, at 0.31 nm per cycle, whereas the growth rate from 3 to 8 ALD cycles was almost constant (0.0002 nm per cycle) and at 8 to 15 ALD cycles it was increasing again (0.10 nm per cycle). This could

be because of rapid and unrestricted diffusion and adsorption of precursors ($TiCl_4$ and water) on the solid surface in the initial period of deposition (1–3 cycles). Further, ALD growth on a rough surface will have a higher GPC, as more material can be deposited per cycle in view of the larger effective surface area that is available for growth (Dendooven and Detavernier 2017). The growth rate remained unchanged, whereas the interstitial atomic spaces decreased with subsequent deposition (3 to 8 ALD cycles), thus restricting further diffusion of precursors into the tiny spaces. After 8 to 15 ALD cycles, the interstitial spaces were crammed by TiO_2, therefore, the fusion of adjacent grain particles increased the growth rate. Similar growth kinetics has been reported in a previous study (Li et al. 2012).

Physico–chemical differences between ALD coated and uncoated membranes

Surface topography and hydrophobicity

Surface roughness values of the uncoated and coated membranes were 71 (Figure 2a) and 63 nm (Figure 2b), respectively. The results from surface roughness indicate that the coated surface was relatively more even than the uncoated surface. The results from surface roughness indicate a relatively smooth surface for the coated membrane compared to the uncoated membrane at 95% confidence level. A smooth surface is ideal for filtration because it limits foulant/pollutant adhesion onto the membrane surface, and subsequently enhances the anti-fouling properties (Motsa et al. 2018). The water contact angles were 59.5° (Figure 2c) and 32.4° (Figure 2d) for uncoated and coated membranes, respectively. Thus coating increased the water affinity of the membrane surfaces, implying the membrane will always be covered by a layer of water, which plays a huge role in water transport and repelling of foulants (Motsa et al. 2014). This improves the anti-fouling properties of the membranes. The hydrophilicity of the coated membrane was likely enhanced by the additional OH groups introduced by the ALD process. The enhancement of hydrophilicity increases water flux because of the improved wettability and reduces membrane fouling by hydrophobic foulants due to diminished adhesive foulant-membrane hydrophobic interactions on the membrane surface (Sun et al. 2013).

The EDS spectra of the selective layer of the uncoated (Figure 2e) and the coated (Figure 2f) membranes showed similar elemental composition for key elements (46.6 and 46.6% Al; 45.6 and 45.1% O and
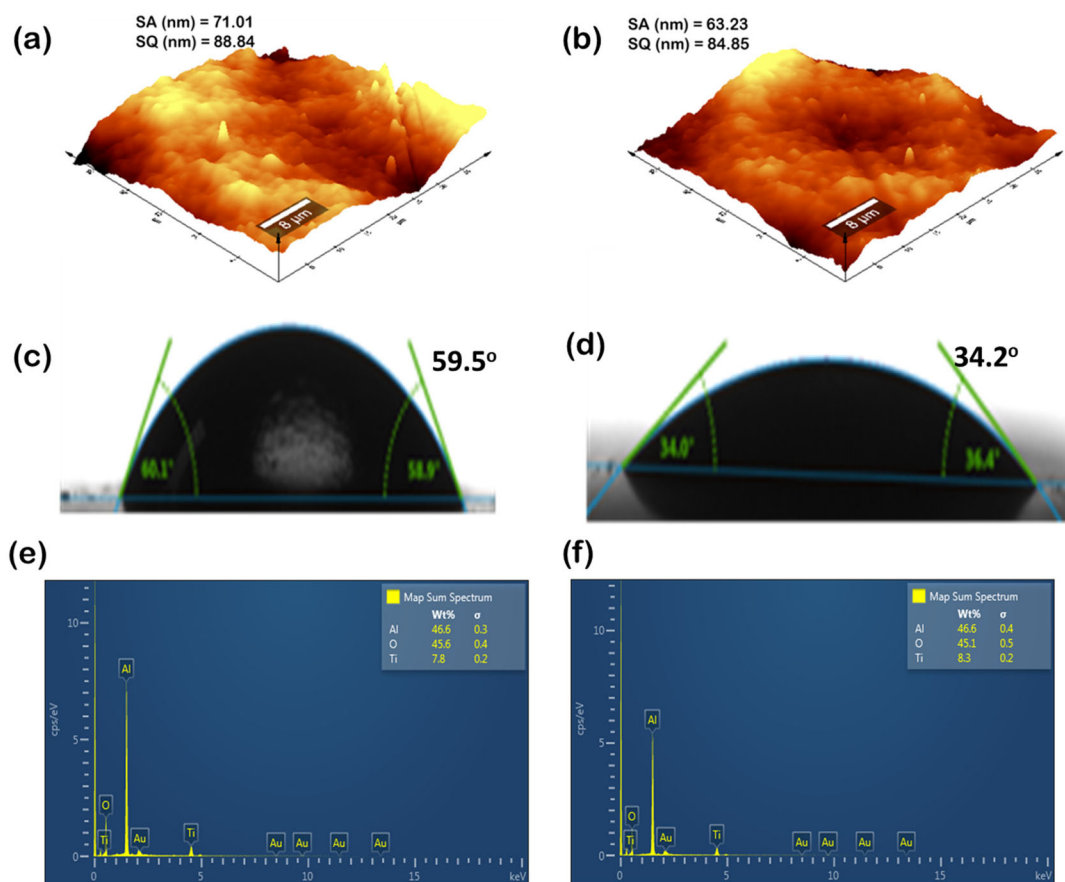
Figure 2. Comparison of the surface topography and chemistry of the uncoated and coated membrane: AFM (a) uncoated and (b) coated; CA (c) uncoated and (d) coated; EDS (f) uncoated and (g) coated.

Table 1. The calculated interfacial free energy components of the uncoated and coated membrane surfaces.

|	Surface free energy components				
	γ^+ (mJm^{-2})	γ^- (mJm^{-2})	γ^{LW} (mJm^{-2})	γ^{AB} (mJm^{-2})	γ^{TOT} (mJm^{-2})
Uncoated	0.24	45.09	38.57	6.62	45.20
Coated	0.36	56.69	35.3	9.06	44.36

γ^{LW} – Liftshitz-van der Waals component; γ^{AB} – Lewis acid–base component; γ^+ – *electron acceptor*; and γ^- – electron donor; and $\gamma^{TOT} - (\gamma^{LW} + \gamma^{AB})$.

7.8 and 8.3% Ti, respectively). This confirms the resultant deposition of a layer with similar elemental composition. Interestingly, Ti did not constitute the elemental composition in the cross sectional morphology of the coated membrane (Supplementary material, Figure S2), suggesting no interior pore modification occurred. Thus, the pore geometry remained unaltered. This was an artefact of the experimental conditions where the pulse time was too short for any penetration of the precursors into the interior of pores. Comparable experimental conditions used in a previous study yielded similar effects (Zhu et al. 2019). Because the pore structure was unchanged, water flow resistance is expected to be unaffected by the coating. Rather, any changes in properties such as water affinity and anti-fouling

would be due to favorable interactions of the additional surface deposited TiO$_2$ and water molecules.

Surface energetics

The monopolarity coefficients of the coated and the uncoated membranes showed strong electron donor properties (Table 1). The water contact angles corroborated the determined surface free energy values. The higher contact angle of the uncoated membrane correlated with the apolar liquid, diiodomethane as evidenced by a higher Lifshitz-van der Waals component (γ). The surface hydrophilicity was enhanced upon coating as shown by the acid-base (γ^{AB}) values, which were 6.62 and 9.06 for the uncoated and ALD coating membranes, respectively. The addition of extra layers of TiO$_2$ at the atomic scale *via* ALD
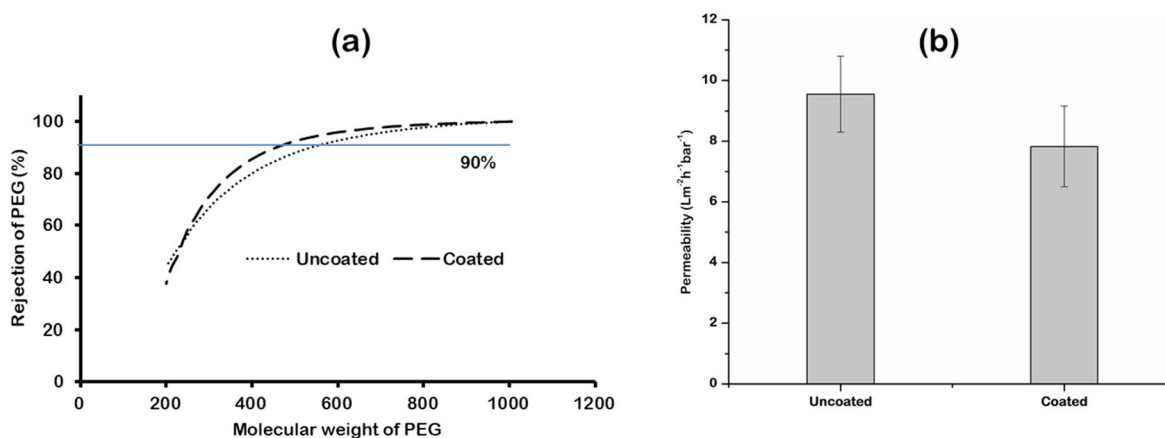
Figure 3. The effect of atomic layer deposition on: (a) MWCO determination, and (b) permeability measurements of the uncoated and the coated membranes.

created favorable conditions which increased the wettability of the surface of the membrane. This consequently lowered the adhesion interaction forces between the surface of the membrane and the oncoming foulants. Accordingly, the propensity of the membrane surface to foul was expected to decrease.

Molecular weight cut off and permeability

The PEG rejection curve was steeper in the region of 200–400 Da for the coated membranes (Figure 3a), suggesting that coating produced homogenous pores with a higher rejection capacity of PEGs (Shang et al. 2017). Further, the three ALD-coating cycles reduced the MWCO by 81 Da (Supplementary material, Figure 3a). From the EDS spectra and the operation conditions, deposition occurred at the surface not the interiors of the pore structures, therefore reduction in MWCO was due to pore aperture constriction. With increasing ALD cycles, the precursors would reach a critical diameter closer to the pore aperture diameter, at which point the pore aperture will restrict the diffusion of the precursors into the interior of the pores (Shang et al. 2017). Therefore, using the current experimental conditions, a significant decrease in MWCO of the membranes beyond three ALD cycles was unlikely. Further, literature reports ALD coatings below 50 cycles give rise to a thicker and denser structure with minimal interior pore constriction (Li et al. 2011).

The three ALD coatings resulted in $1.7 \, Lm^{-2}h^{-1}bar^{-1}$ reductions in permeability. The deposition of TiO_2 via ALD reduced the pore sizes consequently resulting in the observed permeability reduction. The experimental conditions did not allow for deeper penetration of the precursors into the interior of the pores, therefore pore constriction did not occur which would have resulted in even greater

permeability reduction. Literature records that exposure time play a role in the formation of a thicker and denser selective layer, which subsequently impacts the overall permeability of the membrane. For example, Li et al. (2012) compared the effect of exposure time of zero and ten seconds of 200 ALD cycles and found that the permeability difference was 54%. Shang et al. (2017) investigated the effect of five seconds of exposure time after three ALD cycles and found a 58% loss in permeability. Membrane permeability is greatly affected by a deeper impregnation and deposition of TiO_2 which consequently reduces the porosity of the selective layer (Shang et al. 2017). Furthermore, it is possible that longer exposure time could result in the deposition of the precursors in the intermediate and support layer, further constricting the pore diameter consequently resulting in even greater permeability loss. The experimental data suggest the deposition on the surface of the membrane results in negligible permeability losses compared to experiments of prolonged exposure times. In agreement with the literature, Nikkola et al. (2014) deposited between 10 to 100 ALD cycles of Al_2O_3 onto reverse osmosis (RO) membranes, and found that deposition was only restricted to the membrane surface and minor permeability losses occurred for growth below 50 ALD cycles. Beyond 50 ALD cycles the permeability is reduced due to the compaction of the deposited layers.

Remarkably, the ALD-coated membrane showed greater permeability than the reported sol gel synthesized membranes of comparable MWCO. Ceramic membranes of MWCO of 300 Da and synthesized via the sol gel method with ZrO_2 selective layer had a permeability of $2.5 \, Lm^{-2}h^{-1}bar^{-1}$ (Gestel et al. 2006). Therefore, fabrication of tighter NF membranes via ALD methods offers a potentially lucrative alternative
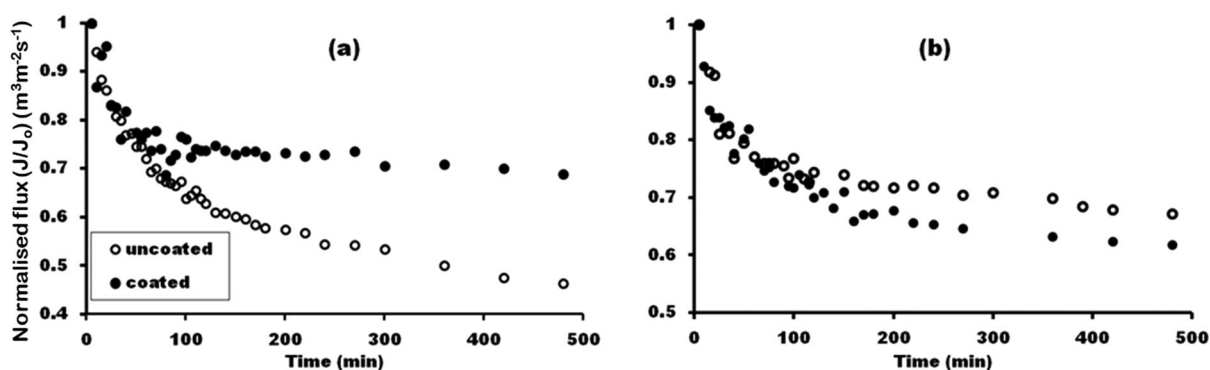
Figure 4. Comparison of permeate flux loss profiles of the uncoated and coated membranes by single and combined model foulants: (a) SA foulant and (b) SA + BSA + HA.
BSA – bovine serum albumin; HA – humic acid; SAL – sodium alginate

as demonstrated by the results. In particular, water permeability is the main economic driver in water treatment practice; it influences capital and operational costs (Hofs et al. 2011). Besides, in water treatment plants, water permeability depends on the physicochemical characteristics of the feed streams, which influences fouling. Membrane fouling in real water samples is due to complex membrane-foulant, foulant-foulant interactions (e.g. calcium-bridged organic fouling, pore narrowing due to adsorption, pore blockage, cake layer formation, etc).

Membrane fouling

### Influence of single foulant on flux loss

Flux decay curves for different foulant combinations on the uncoated membrane are shown in Figure S3 (Supplementary material). The single and combined foulants causing drastic flux loss on the uncoated membrane were SA (54%) and SA + BSA + HA (23%), respectively (Supplementary material, Figure S3). The performance of the ALD coated membrane in mitigating fouling was tested on single and combined foulants.

Previous research indicates SA causes severe fouling, and this is in agreement with the present study (Cheng et al. 2017). There was a 35% flux loss improvement after coating of the membrane when SA was used as the foulant (Figure 4a). The performance of the coated membrane and the uncoated membrane in filtering combined foulants was distinctively different from that of single foulants (Figure 4b). The flux loss profile was influenced by the foulant-foulant and membrane-foulant interactions. The combined foulants flux loss on the uncoated membrane was 23% and the flux loss difference between the coated and the uncoated membrane was 5%, with the uncoated membrane performing better (Figure 4b). Notably,

the flux loss due to the presence of SA was less when in combination than when SA was acting alone. The competitive effect for cations to form bridged complexes might have reduced the formation of bulky SA-SA bridges that could easily settle on the membrane surface (Motsa et al. 2018). This suggests aggregation of SA molecules was minimum, therefore SA remained largely in solution and its chances of settling on the membrane surface were even lower.

The deposition of SA due to permeation drag in the initial stages of filtration onto the membrane surface was enhanced by the more bulky cation bridged SA-SA complexes promoting the adhesion of SA onto the surface of the membrane (Cheng et al. 2017). The coated membrane showed a plateau profile ($m = -0.0426$), indicating the flux decline rate (dj/dt) was more gradual compared to the uncoated membrane ($m = -0.167$) which exhibited a drastic and almost linear flux loss rate ($R^2 = 0.98$) (Figure 5a). Therefore, it was expected that equal contribution of mechanisms of SA fouling would occur on the uncoated membrane.

To quantify the transmission of polysaccharides on the coated and uncoated membrane, the sulfuric acid-UV method was used (Albalasmeh et al. 2013). The UV-visible scans from 200 to 600 nm of samples from the initial feed and permeates from the respective membranes at the end of the experiment runs are presented in Figure 5a insert. The percentage transmission was 45 and 28% for the uncoated and the coated membrane, respectively. The effect of permeation drag was higher on the uncoated membrane compared to the coated membrane due to the difference in MWCO. This implies the polysaccharides were deposited onto the membrane surface at a faster rate on the uncoated membrane than on the coated membrane with greater quantities of polysaccharides passing through the membranes due to wider pores than on the coated membrane. The ALD coating
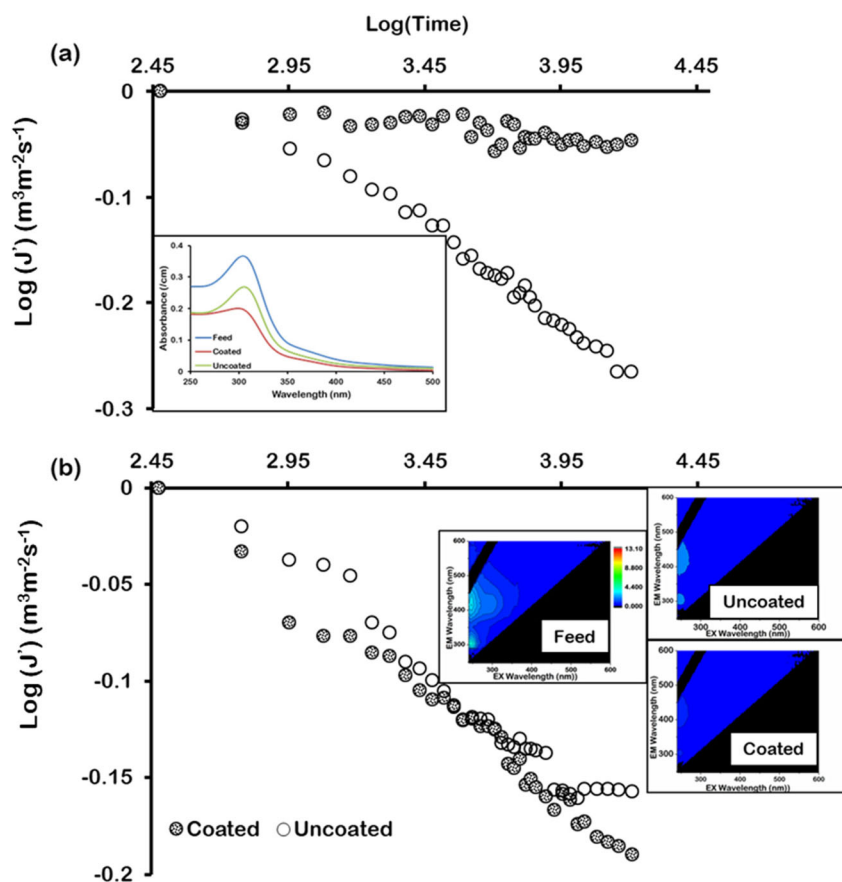
Figure 5. Log transformed flux decline profiles of the coated and uncoated membranes (a) single (SA), with UV absorbance insert. and (b) combined (SA + BSA + HA), with fluorescence emission excitation matrix insert.
BSA – bovine serum albumin; HA – humic acid; SAL – sodium alginate
Log (J') ($m^3m^{-2}s^{-1}$)

reduced the pore aperture of the coated membranes thus restricting the passage of the bulky SA molecules. Further, another possible factor was the electrostatic repulsion of SA by the coated membrane surface due to the introduced OH groups *via* ALD on the surface of the membrane. Further research on zeta potential studies on foulant and membrane surface charges must be carried out to ascertain this finding.

Generally, polysaccharides have a high propensity to foul membranes (Motsa et al. 2014). This is because of their gelling properties that facilitate the adherence of bacterial communities and bulky molecular size that increase filtration resistance. Consequently, polysaccharides pose a challenge in drinking water treatment plants relying on membrane technology. Therefore, efforts to mitigate the impacts of polysaccharides fouling remain a priority in the membrane filtration industry.

Influence of combined foulants on flux loss
The first 60 min showed similar flux loss profiles for both coated and uncoated membranes ($m = -0.108$

and -0.101, respectively) (Figure 5b). The competitive complexation to cations of foulants: BSA-cation, HA-cation, SA-cation, and the severity and settleability of foulant-cation-foulant complexes on the membrane surface occurred to similar extents on membranes. The deposition of these aggregates enhanced permeation loss and reduced the back-diffusion of the deposited salts to the bulk solution. The penultimate 2 h showed a similar flux loss trend for both the coated and uncoated membranes ($m = -0.134$ and -0.102, respectively) (Figure 5b). The slight difference showed that the coated membrane was beginning to foul at a faster rate than the uncoated membrane which showed a very small change. The final 2 h showed distinct flux loss profiles. The uncoated membrane showed a plateau profile ($m = -0.005$), indicating flux decline rate (dj/dt) was less drastic compared to the coated membrane ($m = -0.089$) which exhibited a drastic and almost linear flux loss rate ($R^2 = 0.95$) (Figure 5b). As the experiment progressed, the more bulky foulant-foulant aggregates were deposited
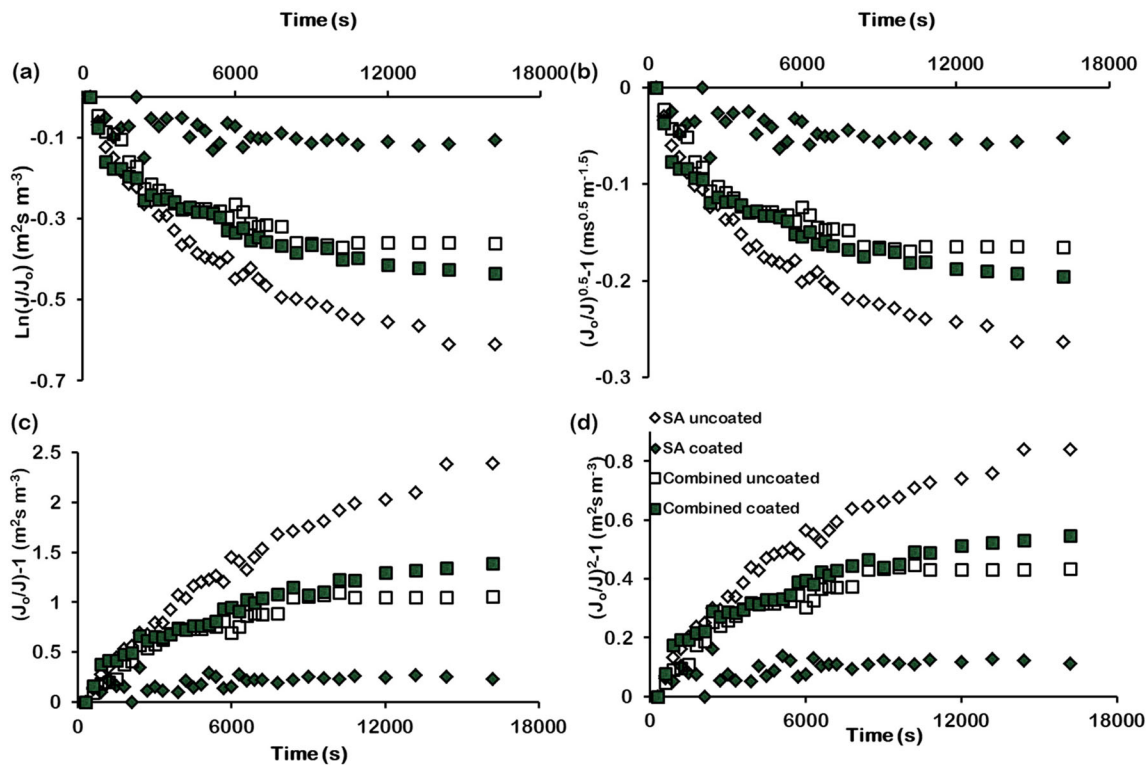
Figure 6. Classic fouling mechanisms due to single (SA) and combined foulants (SA + BSA + HA), on the uncoated and coated membranes: (a) complete, (b) standard blocking, (c) cake filtration, and (d) intermediate fouling.
BSA – bovine serum albumin; HA – humic acid; SAL – sodium alginate

onto the surface of the membrane forming a spongy cake layer.

Figure 5b insert shows the EEM fluorescence spectra of samples from the initial feed and permeates from the respective membranes at the end of the experiment runs. Two distinct peaks and a shoulder were observed; a humic like peak (260/360–450 nm, Ex/Em) of allochthonous terrestrial origin, a humic like shoulder (290–310/370–420 nm, Ex/Em) of autochthonous origin and protein like peak (275/310 nm, Ex/Em) of autochthonous origin (Jiang et al. 2017). The EEMs for the respective permeates showed a decrease in the intensities of the peaks of fluorescent fractions with reference to feed EEM. The humic like peak of autochthonous origin and the protein like peak were retained to at least 80%. The humic like shoulder did not appear on EEM of the permeates, suggesting the humic like matter of autochthonous origin was susceptible to complete the removal by both membranes.

Impact of feed water stream characteristics on fouling mechanisms

Table A2 (Supplementary material) shows the R^2 values denoting the viability of each fouling mechanism. The classic fouling mechanism profiles due to single

and combined foulants on the coated and uncoated membranes are shown in Figure 6.

The flux decline behavior due to SA as the sole foulant on the uncoated membrane is indicative of equal play of all fouling mechanisms and is corroborated by the computed correlation coefficients of each fouling mechanism ($R^2 = 0.98$, 0.98, 0.98 and 0.96 for standard blocking; complete blocking; cake filtration and intermediate blocking, respectively). The R^2 values for the coated membrane with SA as the only foulant were: 0.06, 0.06, 0.82 and 0.17 for complete blocking; standard blocking; cake filtration and intermediate blocking, respectively. The coating compacted the active layer consequently reducing the entrance of the pores, thus, the bulky SA was too bulky to align and deposit at the opening of the pores or further penetrate the pores of the membrane. For this reason, complete blocking, intermediate and standard blocking could not be supported as the likely fouling mechanisms on the coated membrane. However, as the experiment progressed, the bulky SA continuously deposited onto the surface of the membrane, thus suggesting cake filtration as the likely fouling mechanism.

For the combined foulants, the fouling mechanism on the coated and uncoated membranes was almost
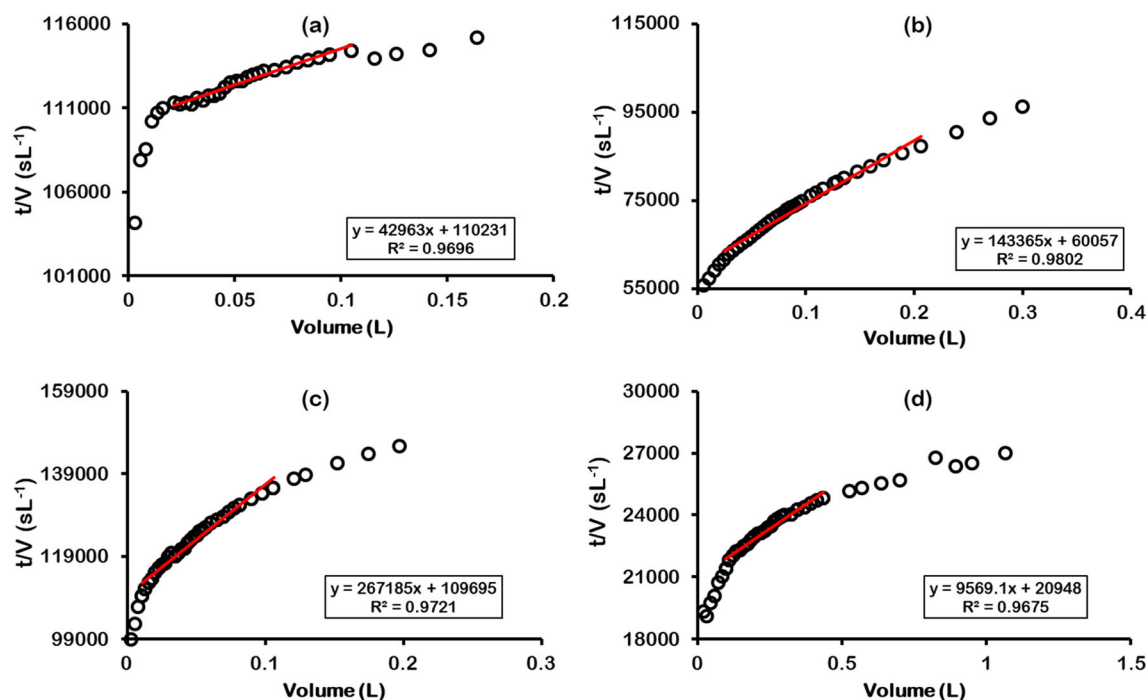
Figure 7. Modified fouling index (MFI) determination for: (a) uncoated membrane due to single foulant (SA), (b) coated membrane due to single foulant (SA), (c) uncoated membrane due to combined foulants (SA + BSA + HA), and (d) coated membrane due to combined foulants (SA + BSA + HA).
BSA – bovine serum albumin; HA – humic acid; SAL – sodium alginate

similar for complete blocking (0.74 and 0.76, respectively), standard blocking (0.74 and 0.75, respectively) and intermediate blocking (0.39 and 0.59, respectively). The competitive effect for cations to form bridged complexes could have reduced the formation of bulky HA-HA and SA-SA bridges that could easily settle on the membrane surface (Motsa et al. 2015). Further, the presence of BSA, which has a relatively smaller in molecular size and higher charge ratio (m/z), means it would attract cations to itself more effectively than the bulkier HA and SAL (Motsa et al. 2018). Thus, because of its m/z, BSA could settle at the opening of the pores and even in the interior of the membranes at almost equal rates for both membranes, hence promoting the aforementioned fouling mechanisms. The likelihood for cake filtration to be the dominant fouling mechanism for the coated and the uncoated membranes was $R^2 = 0.99$ and 0.37; respectively. The results suggest that the introduced OH groups *via* ALD provided more binding sites for cations in the formation of BSA-BSA bridges. Thus, as the experiment progressed, a more compact layer was formed, resulting in hindered back diffusion of salts even in the presence of back diffusive forces arising from cross flow filtration hydrodynamics (cross flow velocity, inertia lift effects and shear). Cake filtration was the least likely fouling mechanism for the uncoated membrane because the heavy foulant-

foulant complexes formed a loose cake layer on the surface of the membrane.

Impact of membrane characteristics and feed stream chemistry on the development of the cake layer

The gradient of the linear segment of the graph of t/V against the cumulative volume of the filtrate, V, denotes the MFI value (Figure 7).

The *MFI* value for the coated and the uncoated membrane upon SA fouling as the sole foulant was 42,963 and 143,365 sL^{-2}, respectively, while the correlation coefficients for cake filtration obtained from the previous section for the respective membranes were 0.82 and 0.98. The combined foulants and the MFI values for the coated and the uncoated membrane were 267,185 and 9569 sL^{-2}, respectively, while the correlation coefficients for cake filtration was 0.99 and 0.37, respectively. The results demonstrate the complementary nature of the two modeling techniques in that the correlation coefficients for the classic fouling mechanisms deduce the likelihood of cake filtration as a dominant fouling mechanism and the MFI model quantifies the extent of cake filtration fouling.

Coating the ceramic membrane reduced the propensity to be fouled by SA *via* cake filtration by 70%. However, coating exacerbated cake filtration fouling

28 times with combined foulants. Previous studies report SA fouling results in a gelatinous and porous cake layer that can easily be detached from the membrane surface by physical means (Motsa et al. 2014). Extended operations without backwashing could have resulted in the deposited SA cake layer attracting bacterial colonies which are more difficult to remove and compromise the physical and chemical integrity of the membrane (Moyo et al. 2019).

Fouling on polymeric membranes was best described using fouling models, in particular, mathematical models fitting cake filtration were developed (Javeed et al. 2009). Research has shown that models such as the MFI can be applied to ceramic membranes to describe cake filtration development upon fouling by DOM (Javeed et al. 2009).

Conclusion

This study demonstrated the antifouling enhancement of ceramic membranes by surface modification *via* atomic layer deposition (ALD) of TiO_2. The main findings were:

- Surface roughness values of the ALD coated and uncoated were 63 and 71 nm, respectively, while the contact angles were 34.2 and 59.5°, respectively. Thus coating increased the water affinity of the membrane surfaces consequently improving the anti-fouling properties.
- The MFI values and the fouling mechanism correlation coefficients for cake filtration for the ALD coated and the uncoated membrane upon alginate fouling were 42,963 ($R^2 = 0.82$) and 143,365 sL^{-2} ($R^2 = 0.98$), respectively, whereas, for the combined foulants, it was 267,185 ($R^2 = 0.99$) and 9569 sL^{-2} ($R^2 = 0.37$), respectively. The results demonstrate the complementary nature of the two modeling techniques. Specifically, the correlation coefficients deduce the likelihood of cake filtration as a dominant fouling mechanism and the MFI model quantifies the extent of cake filtration fouling.

Overall, the research demonstrated that ALD is a potentially viable technique to enhance ceramic membrane antifouling properties.

ORCID

Welldone Moyo http://orcid.org/0000-0003-0341-2919
Titus A. M. Msagati http://orcid.org/0000-0002-9621-5051
Thabo T. I. Nkambule http://orcid.org/0000-0001-9633-1733

References

Albalasmeh AA, Berhe AA, Ghezzehei TA. 2013. A new method for rapid determination of carbohydrate and total carbon concentrations using UV spectrophotometry. Carbohydr Polym. 97:253–261. doi:10.1016/j.carbpol.2013.04.072

Amin SK. 2016. An overview of production and development of ceramic membranes. Int J Appl Eng Res. 11:7708–7721.

Cheng X, Liang H, Ding A, Tang X, Liu B, Zhu X, Gan Z, Wu D, Li G. 2017. Ferrous iron/peroxymonosulfate oxidation as a pretreatment for ceramic ultrafiltration membrane: control of natural organic matter fouling and degradation of atrazine. Water Res. 113:32–41. doi:10.1016/j.watres.2017.01.055

De Angelis L, Cortalezzi MMFd. 2013. Ceramic membrane filtration of organic compounds: effect of concentration, pH, and mixtures interactions on fouling. Sep Purif Technol. 118:762–775. doi:10.1016/j.seppur.2013.08.016

Dendooven J, Detavernier C. 2017. Atomic layer deposition in energy conversion applications. In: Bachmann J, editor. Basics of atomic layer deposition: growth characteristics and conformality. Wiley-VCH Verlag GmbH & Co. KGaA; p. 3–40. doi:10.1002/9783527694822

Fang LF, Kato N, Yang HY, Cheng L, Hasegawa S, Jeon S, Matsuyama H. 2018. Evaluating the antifouling properties of poly(ether sulfone)/sulfonated poly(ether sulfone) blend membranes in a full-size membrane module. Ind Eng Chem Res. 57:4430–4441. doi:10.1021/acs.iecr.8b00114

Gestel TV, Kruidhof H, Blank DH, Bouwmeester HJ. 2006. ZrO2 and TiO2 membranes for nanofiltration and pervaporation Part 1. Preparation and characterization of a corrosion-resistant ZrO2 nanofiltration membrane with a MWCO < 300. J Membr Sci. 284:128–136.

Hofs B, Ogier J, Vries D, Beerendonk EF, Cornelissen ER. 2011. Comparison of ceramic and polymeric membrane

permeability and fouling using surface water. Sep Purif Technol. 79:365–374. doi:10.1016/j.seppur.2011.03.025

Javeed MA, Chinu K, Shon HK, Vigneswaran S. 2009. Effect of pre-treatment on fouling propensity of feed as depicted by the modified fouling index (MFI) and cross-flow sampler-modified fouling index (CFS-MFI). Desalination. 238:98–108. doi:10.1016/j.desal.2008.01.040

Jee KY, Shin DH, Lee YT. 2016. Surface modification of polyamide RO membrane for improved fouling resistance. Desalination. 394:131–137. doi:10.1016/j.desal.2016.05.013

Jiang T, Skyllberg U, Björn E, Green NW, Tang J, Wang D, Gao J, Li C. 2017. Characteristics of dissolved organic matter (DOM) and relationship with dissolved mercury in Xiaoqing River-Laizhou Bay estuary, Bohai Sea, China. Environ Pollut. 223:19–30. doi:10.1016/j.envpol.2016.12.006

Kim H, Oh I. 2014. Review of plasma-enhanced atomic layer deposition: technical enabler of nanoscale device fabrication. Jpn J Appl Phys. 53:03DA01. doi:10.7567/JJAP.53.03DA01

Kimura K, Oki Y. 2017. Efficient control of membrane fouling in MF by removal of biopolymers: comparison of various pretreatments. Water Res. 115:172–179. doi:10.1016/j.watres.2017.02.033

Koo CH, Mohammad AW, Suja F, Meor Talib MZ. 2013. Setting-up of modified fouling index (MFI) and crossflow sampler-modified fouling index (CFS-MFI) measurement devices for NF/RO fouling. J Membr Sci. 435:165–175. doi:10.1016/j.memsci.2013.02.027

Kramer FC, Shang R, Scherrenberg SM, Rietveld LC, Heijman SJG. 2019. Quantifying defects in ceramic tight ultra- and nanofiltration membranes and investigating their robustness. Sep Purif Technol. 219:159–168. doi:10.1016/j.seppur.2019.03.019

Le MH, Kim KJ, Jang A. 2018. Foulant–foulant interaction of combined micro-particulate and organic fouling on a ceramic membrane. KSCE J Civ Eng. 22:4814–4825. doi:10.1007/s12205-018-0611-8

Li F, Li L, Liao X, Wang Y. 2011. Precise pore size tuning and surface modifications of polymeric membranes using the atomic layer deposition technique. J Membr Sci. 385-386:1–9. doi:10.1016/j.memsci.2011.06.042

Li F, Yang Y, Fan Y, Xing W, Wang Y. 2012. Modification of ceramic membranes for pore structure tailoring: the atomic layer deposition route. J Membr Sci. 397-398:17–23. doi:10.1016/j.memsci.2012.01.005

Li P, Hur J. 2017. Utilization of UV-Vis spectroscopy and related data analyses for dissolved organic matter (DOM) studies: a review. Crit Rev Environ Sci Technol. 47:131–154. doi:10.1080/10643389.2017.1309186

Metsämuuronen S, Sillanpää M, Bhatnagar A, Mänttäri M. 2014. Natural organic matter removal from drinking water by membrane technology. Sep Purif Technol. 43:1–61. doi:10.1080/15422119.2012.712080

Motsa MM, Mamba BB, D'Haese A, Hoek EMV, Verliefde ARD. 2014. Organic fouling in forward osmosis membranes: the role of feed solution chemistry and membrane structural properties. J Membr Sci. 460:99–109. doi:10.1016/j.memsci.2014.02.035

Motsa MM, Mamba BB, Verliefde ARD. 2015. Combined colloidal and organic fouling of FO membranes: the influence of foulant–foulant interactions and ionic strength. J Membr Sci. 493:539–548. doi:10.1016/j.memsci.2015.06.035

Motsa MM, Mamba BB, Verliefde ARD. 2018. Forward osmosis membrane performance during simulated wastewater reclamation: fouling mechanisms and fouling layer properties. J Water Process Eng. 23:109–118. doi:10.1016/j.jwpe.2018.03.007

Moyo W, Motsa MM, Chaukura N, Msagati TA, Mamba BB, Heijman SG, Nkambule TT. 2019. Fundamental fouling mechanisms of dissolved organic matter fractions and their implications on the surface modifications of ceramic nanofiltration membranes: insights from a laboratory scale application. Water Sci Technol. 80:1702–1714. doi:10.2166/wst.2019.419

Mustafa G, Wyns K, Buekenhoudt A, Meynen V. 2016. Antifouling grafting of ceramic membranes validated in a variety of challenging wastewaters. Water Res. 104:242–253. doi:10.1016/j.watres.2016.07.057

Nkambule TI. 2012. [Natural organic matter (nom) in South African waters: characterization of nom]. [Treatability and method development for effective nom removal from water. PhD thesis]. University of Johannesburg.

Nikkola J, Sievänen J, Raulio M, Wei J, Vuorinen J, Tang CY. 2014. Surface modification of thin film composite polyamide membrane using atomic layer deposition method. J Membr Sci. 450:174–180. doi:10.1016/j.memsci.2013.09.005

Park J, Kang S, Kim H. 2006. Growth mechanism and diffusion barrier property of plasma-enhanced atomic layer deposition Ti–Si–N thin films. J Vac Sci Technol B. 24:1327–1332. doi:10.1116/1.2198846

Salinas-Rodriguez SG, Amy GL, Schippers JC, Kennedy MD. 2015. The Modified Fouling Index Ultrafiltration constant flux for assessing particulate/colloidal fouling of RO systems. Desalination. 365:79–91. doi:10.1016/j.desal.2015.02.018

Shang R, Goulas A, Tang CY, de Frias Serra X, Rietveld LC, Heijman SGJ. 2017. Atmospheric pressure atomic layer deposition for tight ceramic nanofiltration membranes: synthesis and application in water purification. J Membr Sci. 528:163–170. doi:10.1016/j.memsci.2017.01.023

Sun W, Liu J, Chu H, Dong B. 2013. Pretreatment and membrane hydrophilic modification to reduce membrane fouling. Membranes (Basel). 3:226–241. doi:10.3390/membranes3030226

Sun W, Nan J, Xing J, Tian J. 2016. Identifying the major fluorescent components responsible for ultrafiltration membrane fouling in different water sources. J Environ Sci (China). 45:215–223. doi:10.1016/j.jes.2016.01.007

Tylkowski B, Tsibranska I. 2015. Overview of main techniques used for membrane characterization. J Chem Technol Metall. 50:3–12.

Yu W, Liu T, Crawshaw J, Liu T, Graham N. 2018. Ultrafiltration and nanofiltration membrane fouling by natural organic matter: mechanisms and mitigation by pre-ozonation and pH. Water Res. 139:353–362. doi:10.1016/j.watres.2018.04.025

Zhou Y, Shi K, Zhang Y, Jeppesen E, Liu X, Zhou Q, Wu H, Tang X, Zhu G. 2017. Fluorescence peak integration

ratio IC:IT as a new potential indicator tracing the compositional changes in chromophoric dissolved organic matter. Sci Total Environ. 574:1588–1598. doi:10.1016/j.scitotenv.2016.08.196

Zhou Z, Guo L. 2015. A critical evaluation of an asymmetrical flow field-flow fractionation system for colloidal size characterization of natural organic matter.

J Chromatogr A. 1399:53–64. doi:10.1016/j.chroma.2015.04.035

Zhu Z, Sippola P, Ylivaara OM, Modanese C, Di Sabatino M, Mizohata K, Merdes S, Lipsanen H, Savin H. 2019. Low-temperature plasma-enhanced atomic layer deposition of SiO_2 using carbon dioxide. Nanoscale Res. Lett. 14:1–8. doi:10.1186/s11671-019-2889-y